Technical University of Denmark

DTU

The Reflection Component from Cygnus X-1 in the Soft State Measured by NuSTAR and Suzaku

Tomsick, John A.; Nowak, Michael A.; Parker, Michael; Miller, Jon M.; Fabian, Andy C.; Harrison, Fiona A.; Bachetti, Matteo; Barret, Didier; Boggs, Steven E.; Christensen, Finn Erland; Craig, William W.; Forster, Karl; Fuerst, Felix; Grefenstette, Brian W.; Hailey, Charles J.; King, Ashley L.; Madsen, Kristin K.; Natalucci, Lorenzo; Pottschmidt, Katja; Ross, Randy R.; Stern, Daniel; Walton, Dominic J.; Wilms, Joern; Zhang, William W.

Link back to DTU Orbit

DTU Library
Technical Information Center of Denmark

THE REFLECTION COMPONENT FROM CYGNUS X-1 IN THE SOFT STATE MEASURED BY *NuSTAR* AND *SUZAKU*

JOHN A. TOMSICK[1], MICHAEL A. NOWAK[2], MICHAEL PARKER[3], JON M. MILLER[4], ANDY C. FABIAN[3], FIONA A. HARRISON[5],
MATTEO BACHETTI[6,7], DIDIER BARRET[6,7], STEVEN E. BOGGS[1], FINN E. CHRISTENSEN[8], WILLIAM W. CRAIG[1,9], KARL FORSTER[5],
FELIX FÜRST[5], BRIAN W. GREFENSTETTE[5], CHARLES J. HAILEY[10], ASHLEY L. KING[4], KRISTIN K. MADSEN[5],
LORENZO NATALUCCI[11], KATJA POTTSCHMIDT[12,13], RANDY R. ROSS[14], DANIEL STERN[15],
DOMINIC J. WALTON[5], JÖRN WILMS[16], AND WILLIAM W. ZHANG[17]

[1] Space Sciences Laboratory, 7 Gauss Way, University of California, Berkeley, CA 94720-7450, USA; jtomsick@ssl.berkeley.edu
[2] Massachusetts Institute of Technology, Kavli Institute for Astrophysics, Cambridge, MA 02139, USA
[3] Institute of Astronomy, University of Cambridge, Madingley Road, Cambridge CB3 0HA, UK
[4] Department of Astronomy, University of Michigan, 500 Church Street, Ann Arbor, MI 48109, USA
[5] Cahill Center for Astronomy and Astrophysics, California Institute of Technology, Pasadena, CA 91125, USA
[6] Université de Toulouse, UPS-OMP, IRAP, F-31400 Toulouse, France
[7] CNRS, Institut de Recherche en Astrophysique et Planétologie, 9 Av. colonel Roche, BP 44346, F-31028 Toulouse cedex 4, France
[8] DTU Space, National Space Institute, Technical University of Denmark, Elektrovej 327, DK-2800 Lyngby, Denmark
[9] Lawrence Livermore National Laboratory, Livermore, CA 94550, USA
[10] Columbia Astrophysics Laboratory, Columbia University, New York, NY 10027, USA
[11] Istituto Nazionale di Astrofisica, INAF-IAPS, via del Fosso del Cavaliere, I-00133 Roma, Italy
[12] CRESST and NASA Goddard Space Flight Center, Astrophysics Science Division, Code 661, Greenbelt, MD 20771, USA
[13] Center for Space Science and Technology, University of Maryland Baltimore County, 1000 Hilltop Circle, Baltimore, MD 21250, USA
[14] Physics Department, College of the Holy Cross, Worcester, MA 01610, USA
[15] Jet Propulsion Laboratory, California Institute of Technology, Pasadena, CA 91109, USA
[16] Dr. Karl-Remeis-Sternwarte and Erlangen Center for Astroparticle Physics, Sternwartestrasse 7, D-96049 Bamberg, Germany
[17] NASA Goddard Space Flight Center, Greenbelt, MD 20771, USA

ABSTRACT

The black hole binary Cygnus X-1 was observed in late 2012 with the *Nuclear Spectroscopic Telescope Array* (*NuSTAR*) and *Suzaku*, providing spectral coverage over the ∼1–300 keV range. The source was in the soft state with a multi-temperature blackbody, power law, and reflection components along with absorption from highly ionized material in the system. The high throughput of *NuSTAR* allows for a very high quality measurement of the complex iron line region as well as the rest of the reflection component. The iron line is clearly broadened and is well described by a relativistic blurring model, providing an opportunity to constrain the black hole spin. Although the spin constraint depends somewhat on which continuum model is used, we obtain $a_* > 0.83$ for all models that provide a good description of the spectrum. However, none of our spectral fits give a disk inclination that is consistent with the most recently reported binary values for Cyg X-1. This may indicate that there is a $>13°$ misalignment between the orbital plane and the inner accretion disk (i.e., a warped accretion disk) or that there is missing physics in the spectral models.

Key words: accretion, accretion disks – black hole physics – stars: individual (Cygnus X-1) – X-rays: general – X-rays: stars

Online-only material: color figures

1. INTRODUCTION

Cygnus X-1 (Cyg X-1) is a bright, high-mass X-ray binary that was discovered in the early days of X-ray astronomy (Bowyer et al. 1965) and was identified with the optical counterpart HD 226868 (Murdin & Webster 1971). It is best known for being the first system with a high enough mass measurement to rule out the possibility that the compact object is a neutron star (e.g., Gies & Bolton 1986), making it the first confirmed black hole (BH) system. The current constraint on the BH mass is $14.8 \pm 1.0 \, M_\odot$ (Orosz et al. 2011). Cyg X-1 has been instrumental in improving our understanding of accreting BHs, their spectral states, and the relationship between the accretion disk and the jet (see Remillard & McClintock 2006 for a review of BH binaries).

Currently, a major on-going effort in BH studies is to measure their spins. A non-zero BH spin changes the space time around the BH, requiring the Kerr rather than the Schwarzschild metric to describe the geometry. The spin is also one possible source

for powering the relativistic jets seen coming from BHs. One technique for measuring the BH spin involves modeling the multi-temperature thermal component that comes from the accretion disk (McClintock et al. 2006). A major challenge for this technique is that the distance to the system and the inclination of the inner disk must be known. For Cyg X-1, the distance is well established with a parallax measurement of $1.86^{+0.12}_{-0.11}$ kpc (Reid et al. 2011), which is consistent with a measurement using the dust scattering halo (Xiang et al. 2011). The improved distance determination has also led to new constraints on the binary inclination. Combined modeling of optical spectroscopy (i.e., the companion's radial velocity) and photometry over all orbital phases has given a binary inclination of $27°.1 \pm 0°.8$ (Orosz et al. 2011). Orbital modulations are seen in the optical light curves that depend on the shape of the companion star and the inclination of the system. Although some misalignment between the inner disk inclination and the binary inclination is possible (Maccarone 2002), under the assumption that they are the same, Gou et al. (2011) find that the spin of the

Cyg X-1 BH is $a_* > 0.95$ (3σ limit) and an even higher spin limit ($a_* > 0.983$ at 3σ) has been recently reported (Gou et al. 2013).

Another technique for measuring BH spin involves modeling the Compton reflection component that is due to hard X-ray emission shining on the inner part of the optically thick accretion disk. The reflection spectrum includes fluorescent emission lines, with the Fe Kα lines typically being the strongest (Fabian et al. 1989), and a broad excess in the $\sim$10–50 keV energy range (Lightman & White 1988). The reflection spectrum can be distorted by the relativistic effects of Doppler broadening from the fast orbital motion and the gravitational redshift due to the BH's gravitational field (Fabian et al. 1989). The emission lines can also be broadened when photons are Compton scattered out of the narrow line core (Ross & Fabian 2005). This implies that broad emission lines are not necessarily an indication of relativistic effects. However, the Compton broadening is symmetric, so modeling the asymmetric component is the key to using this technique to constrain BH spin (Reynolds & Nowak 2003; Miller 2007).

For both thermal and reflection component modeling techniques, the BH spin measurement is actually inferred from the measurement of the location of the inner radius of the optically thick and "cold" (i.e., not fully ionized) accretion disk. The BH spin measurement then comes from identifying the inner radius with the innermost stable circular orbit (ISCO). For a non-rotating BH ($a_* \equiv Jc/G(M_{\rm BH})^2 = 0$, where J is the angular momentum of the BH, c is the speed of light, G is the gravitational constant, and $M_{\rm BH}$ is the mass of the BH), the ISCO is at six gravitational radii ($R_g = GM_{\rm BH}/c^2$) and, for a maximally rotating BH ($a_* = 1$), the ISCO approaches 1 R_g.

For Cyg X-1, most of the reflection studies have used X-ray spectra from times when the source was in the hard state. In this state, it is unclear whether the assumption about the inner disk radius being at the ISCO holds. For BH transients, studies allow for the possibility that the disk recedes when the source is in the faint hard state at an Eddington fraction ($L/L_{\rm Edd}$) of $\sim$0.1–0.01% (Nowak et al. 2002; Tomsick et al. 2009; Cabanac et al. 2009), but there is evidence that the disk remains close to or at the ISCO during the bright part of the hard state (Miller et al. 2006; Reis et al. 2010). Historically, Cyg X-1 has been in the bright part of the hard state, making the ISCO assumption plausible. Using hard-state observations, Nowak et al. (2011) did not report a spin measurement but put an upper limit on disk recession. Other reflection-based measurements constrained the BH spin to be $0.6 \leqslant a_* \leqslant 0.99$ (Miller et al. 2012), $a_* = 0.88^{+0.07}_{-0.11}$ (Duro et al. 2011), and $a_* = 0.97^{+0.014}_{-0.02}$ (Fabian et al. 2012a).

The reflection fits in the hard state provide evidence for high BH spin consistent with the limit on the BH spin from thermal modeling in the soft state. In this paper, we report on the details of reflection modeling in the soft state using observations with the *Nuclear Spectroscopic Telescope Array* (*NuSTAR*; Harrison et al. 2013) and *Suzaku* (Mitsuda et al. 2007). *NuSTAR* covers the 3–79 keV bandpass, which is ideal for reflection studies. Its detectors give unprecedented energy resolution in the hard X-ray band and provide high throughput without the photon pile-up that occurs for charge-coupled device (CCD) observations of bright sources. *NuSTAR* has already been used for reflection studies of the supermassive BH NGC 1365 (Risaliti et al. 2013), as well as the Galactic BH GRS 1915+105 (Miller et al. 2013). In this paper, we provide details of the observations, instrument capabilities, and the data reduction
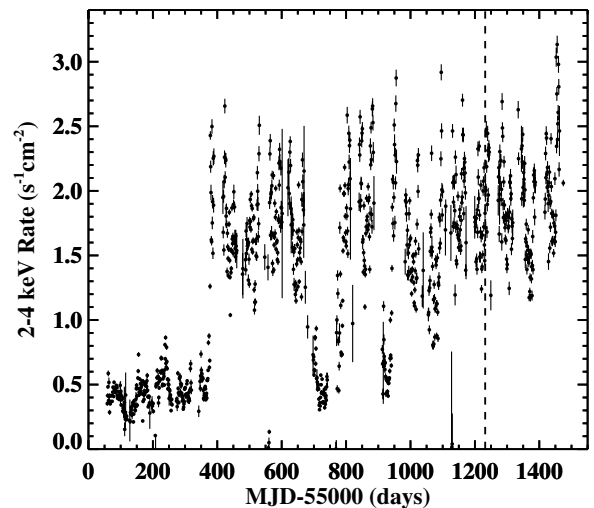

Figure 1. *MAXI* light curve in the 2–4 keV band for Cyg X-1 between mid-2009 and mid-2013. The source was in the hard state until MJD 55,377 and has spent most of its time in the soft state since then. The *NuSTAR* and *Suzaku* observations that are the subject of this work are indicated by a vertical dashed line.

methods in Section 2. The results of the spectral fitting are reported in Section 3 and the results are discussed in Section 4. Finally, we present conclusions in Section 5.

2. OBSERVATIONS AND DATA REDUCTION

We observed Cyg X-1 with *NuSTAR* and *Suzaku* on 2012 October 31 and November 1 (MJD 56,231 and 56,232). Figure 1 shows the soft X-ray light curve from the *Monitor of All-sky X-ray Image* (*MAXI*; Matsuoka et al. 2009), indicating how this observation fits into the $\sim$4 yr history of this source. At the time of the observation, the *MAXI* 2–4 keV count rate (normalized by effective area) was 1.83 ± 0.04 s^{-1} cm^{-2} and the 4–10 keV count rate was 0.55 ± 0.02 s^{-1} cm^{-2} (obtained from the *MAXI* Web site[18]), demonstrating that the source was in the soft state based on the *MAXI* count rate and hardness criteria determined by Grinberg et al. (2013).

2.1. NuSTAR

We reduced the data from the two *NuSTAR* instruments, Focal Plane Modules (FPMs) A and B, and the exposure times and other observation details are listed in Table 1. The *NuSTAR* FPMs are cadmium–zinc–telluride pixel detectors with an energy resolution (FWHM) of 0.4 keV at 10 keV and 0.9 keV at 68 keV (Harrison et al. 2013). Each FPM is at the focus of a hard X-ray telescope with a focal length of 10.14 m and an angular resolution (half-power diameter) of 58″ (Harrison et al. 2013). We processed the *NuSTAR* data (ObsIDs 30001011002 and 30001011003) with version 1.1.1 of the NuSTARDAS pipeline software, the 2013 May 9 version of the *NuSTAR* Calibration Database (CALDB), and High Energy Astrophysics Software (HEASOFT) version 6.13. We produced cleaned event lists with the routine nupipeline and light curves and spectra with nuproducts. The source extraction region is centered on Cyg X-1 and has a radius of 200″. The background region is a 90″ circle that is taken from the part of the *NuSTAR* field of view that is farthest from the source. For

---

[18] See http://maxi.riken.jp/top/.

2

Table 1
Observing Log and Exposure Times

Mission	Instrument	ObsID	Start Time (UT) (in 2012)	End Time (UT) (in 2012)	On-Source Time (ks)	Exposure (s)
NuSTAR	FPMA	30001011002	Oct 31, 8.18 hr	Oct 31, 17.77 hr	18.4	10,442
NuSTAR	FPMB	"	"	"	"	10,811
NuSTAR	FPMA	30001011003	Oct 31, 17.77 hr	Nov 1, 0.27 hr	10.3	5,096
NuSTAR	FPMB	"	"	"	"	5,257
Suzaku	XIS0	407072010	Oct 31, 8.20 hr	Nov 1, 2.62 hr	30.1	1,939
Suzaku	XIS1	"	"	"	"	1,991
Suzaku	HXD/PIN	"	"	"	"	30,074
Suzaku	HXD/GSO	"	"	"	"	27,880

ObsID 30001011002, the centers of the two regions are $10\rlap{.}'5$ apart and, for ObsID 30001011003, they are separated by $9\rlap{.}'1$. While the background rate is known to vary across the field of view at low energies (Harrison et al. 2013), the source rate is 25–1000 times the background below 30 keV, so systematic errors in the background cannot affect our results over this energy band. At higher energies (combining the energy bins above 30 keV), the source is 21 times the background rate, so small detector-to-detector variations in the background are not important.

2.2. Suzaku

Suzaku covers the ∼0.3–600 keV band via three detectors: the X-ray imaging spectrometers (XISs; Koyama et al. 2007), which are CCDs, the hard X-ray detector (HXD; Takahashi et al. 2007) positive intrinsic negative (PIN) diode detector, and the HXD gadolinium silicate crystal detector (GSO). These instruments cover the ∼0.3–10 keV, the ∼10–70 keV, and the ∼60–600 keV bands, respectively. In this paper, for the XIS, we only consider the XIS0 and XIS1 detectors. During our observation, XIS3 was operated in a continuous readout mode (PSUM mode), complicating its analysis, while XIS2 has not been operational since 2006.

To create spectra from the *Suzaku* data (ObsID 407072010), we used tools from the HEASOFT version 6.13 package and the calibration files current as of 2013 February. We followed the standard procedure for analyzing the XIS spectra, which included correcting for charge transfer inefficiency and reprocessing the data with the xispi and xselect tools, respectively. Thermal bending of the spacecraft leads to attitude uncertainties, which in turn lead to distortions of the point spread function (PSF) image as observed by XIS. Although the standard HEASOFT tools apply corrections to the spacecraft attitude in order to improve the PSF image (Uchiyama et al. 2008), we further correct this image using the aeattcor2 tool, as described by Nowak et al. (2011).

The XIS spectra were obtained in a mode where only 1/4 of the CCD was exposed with each CCD readout frame being 2 s. The spectra, however, were only exposed for 0.135 s per readout frame in order to reduce telemetry and minimize pile up. Despite these precautions, given the brightness of Cyg X-1 in its soft state, the spectra are heavily piled up. To estimate the degree of pile up, we employed the pile_estimate.sl S-Lang script (see Nowak et al. 2011). Using this script, we identified the most heavily piled regions on the CCD and excluded two rectangular regions in the center each measuring approximately 130×45 pixels. We estimate that the remaining regions on the XIS CCDs have an effective pile-up fraction of $\lesssim$5%. We then used xisrmfgen and xissimarfgen to create response matrices for the extracted spectra. To account for systematics, we added a 2%

uncertainty on the XIS spectra in quadrature with the statistical uncertainties.

Standard procedures, following the *Suzaku ABC Guide*,[19] were used to create HXD spectra. PIN spectra were extracted from the hxd/event_cl directories with response and background files downloaded from the pinxb_ver2.0_tuned directory at the High Energy Astrophysics Science Archive Research Center (HEASARC).[20] GSO spectra were created from "unfiltered" event files using the hxdtime, hxdpi, and hxdgrade tools and the filtering criteria from the standard gso_mkf.sel script. The background was obtained from the gsonxb_ver2.0 directory at HEASARC. Event and background file Good Time Intervals were merged to obtain the extraction times for the GSO spectra. Standard CALDB response files were applied to the spectra with their exposure times adjusted to agree with the spectra. The grouping of the GSO spectra followed the fixed grouping of the background file and thus were not rebinned further.

3. RESULTS

Figure 2 shows the 3–79 keV *NuSTAR* and 0.5–9 keV XIS light curves. There is good overlap in the coverage between the two satellites; however, their Earth occultations are not exactly in phase and the *Suzaku* coverage extends somewhat beyond that of *NuSTAR*'s. Flaring, which is typical of Cyg X-1 in this state, is more evident in *NuSTAR*'s hard X-ray band than in the softer X-ray regime covered by XIS. Perhaps the most notable feature in the XIS light curves are brief drops in the count rate. It is possible that these are absorption dips due to material in the massive donor star's stellar wind. This is plausible because the observations occurred at a binary orbital phase of 0.85–0.97 (where 1.0 corresponds to superior conjunction when the donor star is between the observer and the BH) based on the ephemeris of Brocksopp et al. (1999). Absorption dips are typically seen in this range of orbital phase (Bałucińska-Church et al. 2000; Poutanen et al. 2008).

In order to determine the level of spectral variation during the observations, we extracted the 3–10 keV and 10–79 keV *NuSTAR* count rates and produced a plot of hardness, which is the 10–79 keV count rate divided by the 3–10 keV count rate, versus time (Figure 2(c)). Even during the flares, we see little variability in the hardness. Given the relatively low level of spectral variability, we combined all of the data into a single spectrum.

Due to the high count rate for Cyg X-1, the XIS spectra show features that we suspect are related to photon pile up. An upturn

---

[19] See http://heasarc.gsfc.nasa.gov/docs/suzaku/analysis/abc/.
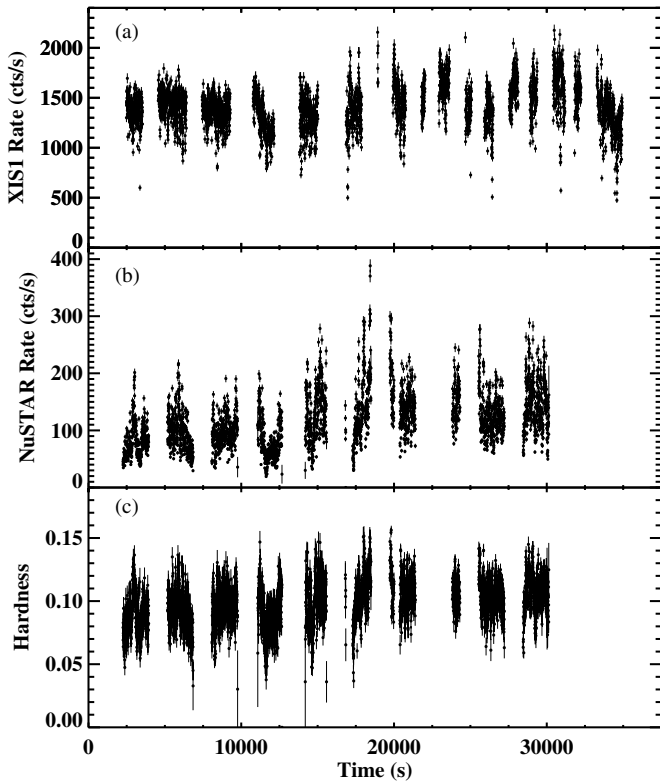[20] See http://heasarc.gsfc.nasa.gov/.

Figure 2. (a) *Suzaku*/XIS light curve, (b) *NuSTAR*/FPMA light curve, and (c) *NuSTAR* hardness ratio for Cyg X-1. For XIS, the bandpass is 0.5–9 keV, and the rate is for XIS1 (after removing the piled-up core of the PSF). For the *NuSTAR* light curve, the bandpass is 3–79 keV, the rate is for FPMA, and it is corrected for dead time. The *NuSTAR* hardness ratio is the 10–79 keV rate divided by the 3–10 keV rate and both modules are used. The time resolution for all plots is 10 s. The zero time is arbitrary but corresponds to MJD 56,231.30000. For both satellites, most of the gaps are due to Earth occultation, but the longer gap near time 22,500 s for *NuSTAR* is due to a missed ground station pass.

Figure 3. Data-to-model ratio for a fit to the Cyg X-1 spectrum with an absorbed disk blackbody plus power-law model (model 1). The panel (a) residuals indicate a strong reflection component. Panel (b) focuses on the iron Kα line region, showing that the line complex includes at least a broad emission component and an absorption line at 6.7 keV.

(A color version of this figure is available in the online journal.)

in the spectra above ∼9 keV is observed and is readily explained by pile up. The spectrum below 1.2 keV shows features that appear to be absorption lines; however, we cannot rule out the possibility of some distortion due to instrumental effects and we defer a detailed study to a later paper. In addition, there are known calibration uncertainties in the 1.7–2.1 keV band related to the Si K edge. After these considerations, for XIS0 and XIS1, we used the 1.2–1.7 keV and 2.1–9 keV bands for spectral analysis and binned the data based on the instrumental energy resolution (see Nowak et al. 2011). For PIN and GSO, we used the 15–68 keV and 50–296 keV energy ranges, respectively. For *NuSTAR*, we used 3–79 keV energy range and binned the spectra for FPMA and FPMB separately, requiring that each bin have a signal-to-noise ratio of at least 30 (after background subtraction).

We used the XSPEC software package (Arnaud 1996) to fit the combined *NuSTAR* plus *Suzaku* spectrum with a model consisting of a multi-temperature "disk blackbody" thermal component (Mitsuda et al. 1984) plus a power law (model 1). These continuum components were subject to absorption with the tbabs model and we used Wilms et al. (2000) abundances and Verner et al. (1996) cross sections for this interstellar absorption. We included a multiplicative constant as a free parameter for each instrument to account for differences in overall normalization. Figure 3 shows the XIS and *NuSTAR* residuals for this fit in terms of the data-to-model ratio, revealing a strong reflection component with a broad iron Kα emission
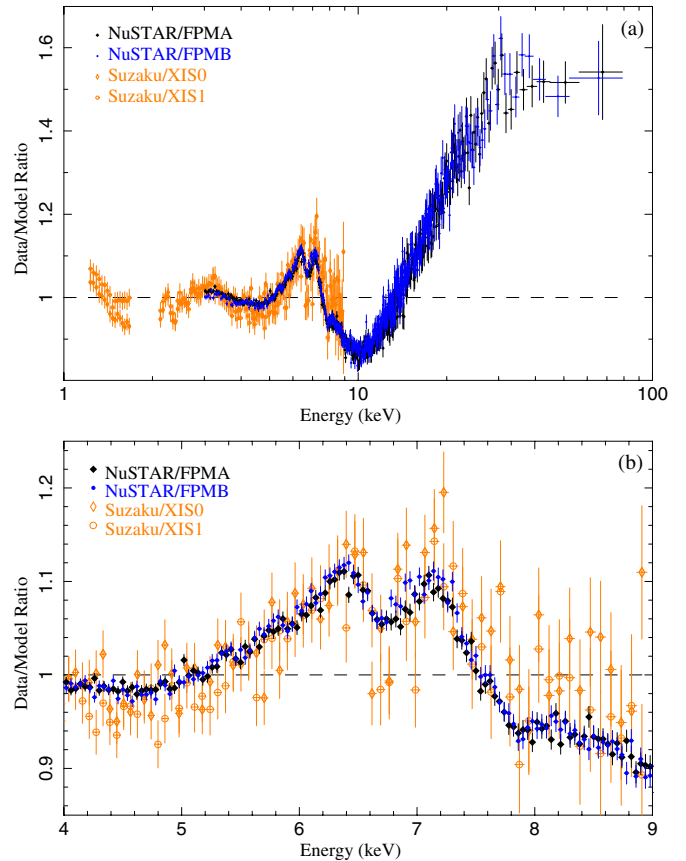
line and a reflection hump above ∼15 keV. Figure 3(b) illustrates the complexity of the iron line, which has an absorption line at 6.7 keV in addition to the broad line in emission.

The fit can be significantly improved with the addition of a Gaussian emission line and a cutoff at high energies (model 2), using highecut, which provides an exponential cutoff with a folding energy of E_{fold} for energies greater than a cutoff energy, E_{cut}. If the Gaussian parameters are allowed to take any values, the line centroid is near 5.3 keV, which is well below the 6.4–7.1 keV iron regime, and the line is extremely broad ($\sigma = 1.57$ keV). In addition to the Gaussian parameter values being unphysical, this model does not give a formally acceptable fit with a reduced χ^2 (χ^2_ν) of 2.00 for 1149 degrees of freedom (dof). The continuum parameters (e.g., a best-fit inner disk temperature of $kT_{in} = 0.62$ keV and a power-law photon index of $\Gamma = 2.5$) are consistent with the source being in the soft state. This model gives absorbed and unabsorbed 0.5–100 keV fluxes of 4.33×10^{-8} erg cm^{-2} s^{-1} and 6.09×10^{-8} erg cm^{-2} s^{-1}, respectively. For a source distance of 1.86 kpc, this implies a luminosity of 2.5×10^{37} erg s^{-1}, which, for a BH mass of 14.8 $M_\odot$, gives an Eddington-scaled luminosity of 1.3%.

As shown in Figure 4(a), the largest residuals for model 2 are in the 6–8.5 keV part of the spectrum. In addition to the fact that we are still not modeling the 6.7 keV absorption line, which is due to the photoionized wind of the massive companion star, a Gaussian is too simple to fit the broad emission feature and the
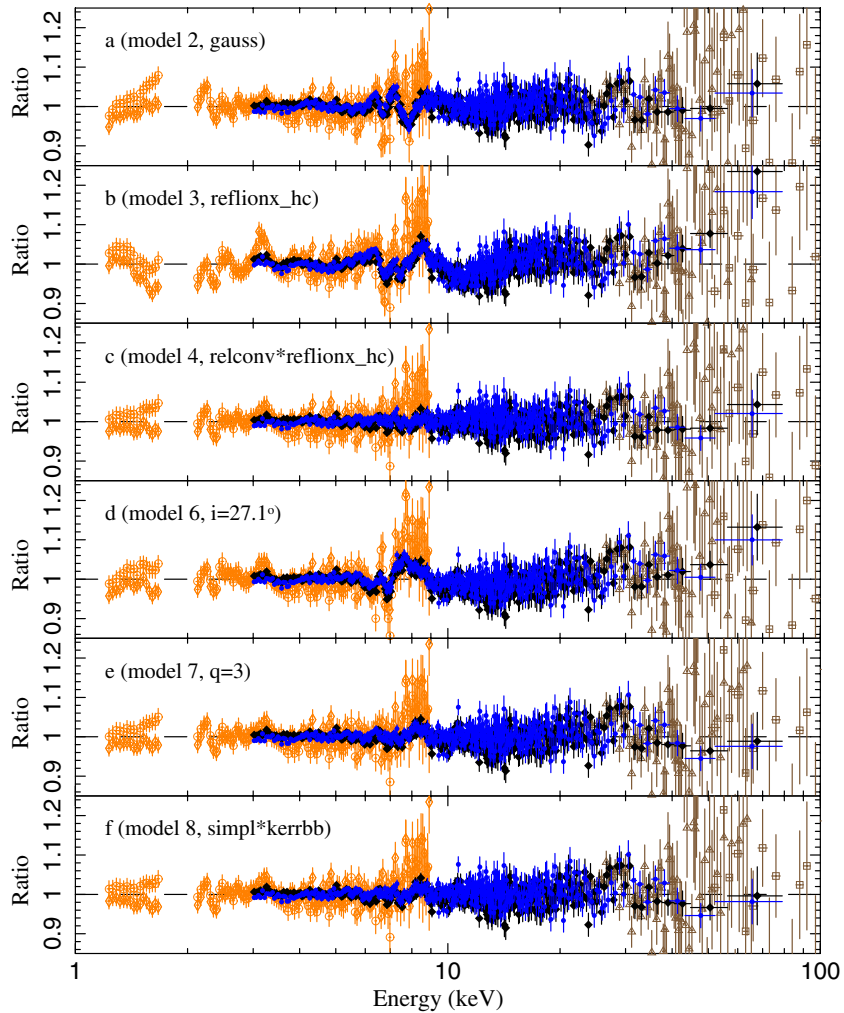
Figure 4. Data-to-model ratios for six of the models described in Section 3. The symbols and colors for XIS0, XIS1, FPMA, and FPMB are the same as in Figure 3. In addition, at higher energies, the PIN and GSO ratios, which are only shown up to 100 keV, are indicated by brown triangles and squares, respectively.
(A color version of this figure is available in the online journal.)

absorption edge that are present in the reflection component. Thus, we removed the Gaussian and added a simple ionized absorber and a reflection component (model 3).

For absorption due to the wind, we constructed a grid of table models using XSTAR version 2.2.1bg (Kallman & Bautista 2001). Solar abundances were assumed for all elements, the number density was fixed at $n = 10^{12}$ cm^{-3}, and the turbulent velocity of the gas was fixed at $v_{turb} = 300$ km s^{-1} (e.g., Miller et al. 2005; Hanke et al. 2009). We used an input spectrum consistent with model 1 described above in order to construct a grid spanning $2 \leqslant \log(\xi) \leqslant 5$, where ξ is the ionization parameter in units of erg cm s^{-1} and 1.0×10^{21} cm$^{-2} \leqslant N_H \leqslant 5.0 \times 10^{22}$ cm^{-2}, where N_H is the column density of the absorber. In total, 400 grid points were calculated and summed into a multiplicative table model that was included in XSPEC analysis, with N_H, ξ and v/c as variable parameters. Although v/c was originally left as a free parameter, we found a 90% confidence upper limit of <0.0004 and we fixed it to zero in the fits described below. This parameter is driven by the strong absorption line at 6.7 keV, which is due to Fe XXV.

For the reflection, we used the `reflionx` model (Ross & Fabian 2005). This model includes the hard X-ray bump, the absorption edges, and the emission lines, so that the full reflection component is physically self-consistent. In addition,

the emission lines are Compton broadened (see Section 1). The version that is available online[21] has the folding energy for its exponential cutoff fixed at 300 keV, but, for our fits, a new model, `reflionx_hc`, was produced with E_{fold} as a free parameter. For the direct component, the `highecut` parameters were set to be consistent with `reflionx_hc`: E_{cut} was set to zero and E_{fold} was forced to have the same value as the free parameter in the reflection model. One other difference between `reflionx` and `reflionx_hc` is that the ionization parameter was extended to higher levels based on early fits to the Cyg X-1 spectrum. While this is a more realistic physical model than using the Gaussian to fit the iron line, model 3 provides a worse fit ($\chi_\nu^2 = 2.72$ for 1148 dof) than model 2 and large residuals are still present in the 5–9 keV regime.

A major improvement in the fit (to $\chi_\nu^2 = 1.21$ for 1143 dof) comes from convolving the reflection component with a relativistic blurring model (model 4). For blurring, we used the `relconv` model (Dauser et al. 2010), which is based on the physics described in Fabian et al. (1989) and Laor (1991), but `relconv` allows for a range of spin values. For these fits, we assume that the accretion disk extends to the ISCO and the blurring, which is most apparent in its effect on the iron line

---

[21] See http://heasarc.gsfc.nasa.gov/xanadu/xspec/models/reflion.html.

Table 2
Fit Parameters for Models Assuming a Disk Blackbody

Parameter	Unit/Description	Model 4 Value[a]	Model 5 Value[a]	Model 7 Value[a]
Interstellar absorption				
$N_{\rm H}$	10^{21} cm^{-2}	6.0 ± 0.3	6.2 ± 0.2	6.2 ± 0.2
Disk blackbody				
$kT_{\rm in}$	keV	$0.558^{+0.004}_{-0.002}$	0.558 ± 0.003	$0.557^{+0.004}_{-0.002}$
$N_{\rm DBB}$	Normalization	$20{,}800^{+1200}_{-800}$	$19{,}600^{+800}_{-600}$	$19{,}600^{+1000}_{-900}$
Cutoff power law				
Γ	Photon index	$2.589^{+0.005}_{-0.022}$	2.66 ± 0.02	2.672 ± 0.014
$N_{\rm pl}$	Normalization[b]	6.0 ± 0.4	$6.8^{+0.4}_{-0.2}$	7.4 ± 0.3
$E_{\rm fold}$	keV	120^{+20}_{-10}	190^{+20}_{-10}	200^{+50}_{-20}
Simple ionized absorber				
$N_{\rm H}$	10^{22} cm^{-2}	$3.45^{+0.14}_{-0.23}$	$3.31^{+0.29}_{-0.10}$	2.86 ± 0.17
$\log \xi$	erg cm s^{-1}	$5.0^{+0.0}_{-0.2}$	$4.84^{+0.16}_{-0.02}$	$5.00^{+0.00}_{-0.03}$
Reflection component (`reflionx_hc`)				
ξ	erg cm s^{-1}	$18{,}100^{+1900}_{-4200}$	$20{,}000^{+0}_{-500}$	$20{,}000^{+0}_{-800}$
Fe/solar	Abundance	2.9 ± 0.4	1.9 ± 0.2	$1.93^{+0.13}_{-0.23}$
$N_{\rm ref}$	Normalization ($\times 10^{-6}$)	$5.955^{+0.003}_{-0.327}$	$6.6^{+0.5}_{-0.4}$	$6.0^{+0.5}_{-0.3}$
Relativistic blurring (`relconv`[c])				
$q_{\rm in}$	Emissivity index	$10.0^{+0.0}_{-0.4}$	$10.0^{+0.0}_{-0.5}$	3.0[d]
$q_{\rm out}$	Emissivity index	$-1.2^{+1.1}_{-4.6}$	10.0	3.0[d]
$R_{\rm break}$	Index break radius ($R_{\rm g}$)	10^{+15}_{-3}	$\cdots$	$\cdots$
a_*	BH spin	0.9882 ± 0.0009	$0.91^{+0.01}_{-0.02}$	0.75 ± 0.05
i	Inclination (deg)	$69.2^{+0.5}_{-0.9}$	$59.3^{+0.5}_{-1.3}$	42.4 ± 0.5
Cross-normalization constants (relative to FPMA)				
$C_{\rm XIS0}$	$\cdots$	1.081 ± 0.005	1.082 ± 0.005	1.081 ± 0.005
$C_{\rm XIS1}$	$\cdots$	1.038 ± 0.005	1.039 ± 0.005	1.038 ± 0.005
$C_{\rm FPMB}$	$\cdots$	1.001 ± 0.001	1.001 ± 0.001	1.001 ± 0.001
$C_{\rm PIN}$	$\cdots$	1.202 ± 0.006	1.204 ± 0.006	1.207 ± 0.007
$C_{\rm GSO}$	$\cdots$	1.23 ± 0.06	1.17 ± 0.05	1.16 ± 0.05
χ^2/ν	$\cdots$	$1388/1143$	$1501/1145$	$1610/1146$

Notes.
[a] With 90% confidence errors. A value of zero for the positive error indicates that the parameter's error range reached the upper limit of values provided for the model.
[b] In units of ph s^{-1} cm^{-2} keV^{-1} evaluated at 1 keV.
[c] Two other parameters in this model are the inner and outer radii from where the reflected emission is coming: $R_{\rm in}$ is set to be at the ISCO and $R_{\rm out} = 400\ R_{\rm g}$.
[d] Fixed.

shape, depends on the BH spin (a_*), the disk inclination (i), and the radial dependence of the emissivity of reflected flux. The emissivity is assumed to have a power-law shape ($L \propto r^{-q}$, where L is the luminosity illuminating the reflecting material, r is the radial distance from the BH, and q is the emissivity index) or broken power-law shape. The fit parameter values for the broken power-law emissivity (model 4) and for the power-law emissivity (model 5) are given in Table 2 and Figure 5(a) shows the components of the former model.

The fit parameters indicate reflection off highly ionized material ($\xi > 13{,}900$ erg cm s^{-1} for model 4 and $\xi > 19{,}500$ erg cm s^{-1} for model 5) and a steep emissivity index ($q > 9.5$). In addition, we find a high BH spin of $a_* = 0.9882 \pm 0.0009$ for model 4 and $a_* = 0.91^{+0.01}_{-0.02}$ for model 5. These are 90% confidence statistical errors and it is important to note that they do not include any systematic component. The inclinations obtained are $i = 69.2^{+0.5}_{-0.9}$ deg and $i = 59.3^{+0.5}_{-1.3}$ deg for models 4 and 5, respectively, both of which are significantly different from the value of 27°.1 measured for the binary (Orosz et al. 2011). If we fix the inclination to the binary value and

refit the spectrum, we obtain a very poor fit with $\chi^2_\nu = 2.45$ for 1144 dof even for the case of broken power-law emissivity; the residuals are shown in Figure 4(d, model 6). Furthermore, we made error contours[22] for the spin and inclination parameters for model 4 (see Figure 6). Although there is some correlation between these parameters and a nearby local minimum exists, the 3σ contours do not extend below $i \sim 65°.8$.

For all the models presented thus far, if $q_{\rm in}$ is left as a free parameter, we obtain values close to 10, which is the maximum of the allowed range. We also explored the implications of lower emissivity index by fixing it to $q = 3$. This gives $\chi^2_\nu = 1.40$ for

---

[22] To explore correlations among parameters, we performed Markov Chain Monte Carlo (MCMC) simulations with a code modeled after the "emcee hammer" code described by Foreman-Mackey et al. (2013), which implements the algorithm of Goodman & Weare (2010). In this algorithm, an ensemble of "walkers," which are vectors of the fit parameters, are evolved via random steps determined by the difference between two walkers. We evolved 20 walkers per free parameter for a total of 4000–10,000 steps and ignored the first half of the steps. Thus, probability distributions were calculated from $(0.4$–$1.5) \times 10^6$ values. Error contours are the two-dimensional projection of the MCMC N-dimensional probability distribution.
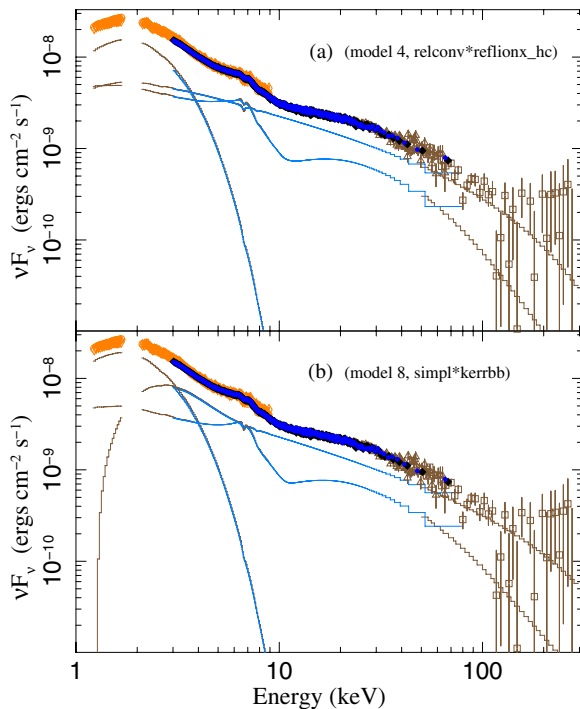
Figure 5. (a) Unfolded *NuSTAR* and *Suzaku* spectrum showing the fit obtained with model 4, which includes a disk blackbody component, a cutoff power law, a `reflionx_hc` reflection model with relativistic blurring, and a simple ionized absorber. (b) The spectrum for model 8, which models the thermal component with `kerrbb` and is self-consistent in that the thermal component is the seed photon distribution for the Comptonized component (using `simpl`). The symbols and colors for the different instruments are the same as for Figure 4.

(A color version of this figure is available in the online journal.)

1146 dof, which is significantly worse than the high-q (and high-i) fit, but the inclination is $42.4^{+0.4}_{-0.5}$ deg, which is much closer to the binary value. The residuals for this model are shown in Figure 4(e, model 7) and the parameters are given in Table 2. Although the BH spin is somewhat lower for model 7, the relatively poor fit suggests that this value is not reliable. For model 4, we left $q_{\rm out}$ as a free parameter and a value of $-1.2^{+1.1}_{-4.6}$ is obtained, indicating that, beyond 10 $R_{\rm g}$, the flux incident on the disk is actually increasing with radius. Although such a rising profile could occur over some range of radii, we note that it is non-physical for the emissivity to continue to increase with radius indefinitely.

While the parameter and BH spin constraints above rely only on modeling the reflection component, a previous Cyg X-1 spin measurement obtained by fitting the soft state spectrum relied primarily on modeling the thermal component (Gou et al. 2011, 2013). Rather than using the disk blackbody model, they used the model `kerrbb`, which is a multi-temperature thermal accretion disk model that accounts for changes in the inner disk (e.g., the inner radius) due to the BH spin. Also, instead of adding a power law, they used the convolution model `simpl` (Steiner et al. 2009), which is different from the disk blackbody plus power-law model described above because it uses the `kerrbb` component as the seed photon input to the Comptonization region. With this model, we obtain $\chi^2_\nu = 1.32$ for 1146 dof. The residuals are shown in Figure 4(f, model 8) and the model components are shown in Figure 5(b). The parameter values from the fit are given in Table 3. The constraint on the spin parameter, $a_* = 0.838 \pm 0.006$, comes from both the thermal component and the reflection component and the inclination ($i = 53\overset{\circ}{.}9 \pm 0\overset{\circ}{.}4$) is still significantly higher than the binary value. Model 8 uses a single power law for the emissivity with an index of $q = 7.8 \pm 0.5$. Figure 6 shows the error contours for spin and inclination for model 8.

Although we do not focus on calibration details in this paper, there is excellent agreement between FPMA and FPMB with the relative normalization being consistent to within 0.1% for all the spectral models described above, which is actually better than expected. Relative to the *NuSTAR*/FPMA, we find normalization constants of 1.081 ± 0.005 for XIS0, 1.038 ± 0.004 for XIS1, 1.205 ± 0.007 for PIN, and 1.17 ± 0.06 for GSO. These numbers are for model 8, but Tables 2 and 3 show very similar relative normalizations for all models. Thus, there is very good agreement between *NuSTAR* and XIS and the fact that PIN and GSO are somewhat higher is expected.[23]

4. DISCUSSION

The combination of *NuSTAR* and *Suzaku* provides a measurement of the Cyg X-1 reflection spectrum with unprecedented quality. While *NuSTAR* measures the entire reflection component (iron line, absorption edges, and hard X-ray bump), the XIS provides an extension to lower energies that is essential for constraining the thermal component. *NuSTAR* and XIS agree to a remarkable extent on the shape of the iron line (see Figure 3(b))
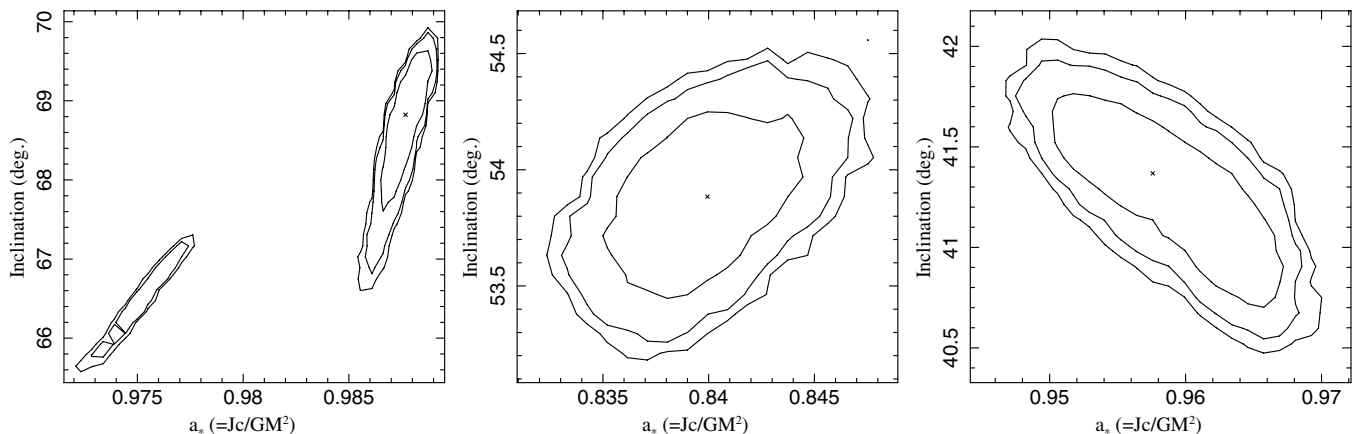
---

[23] See http://www.astro.isas.jaxa.jp/suzaku/doc/suzakumemo/suzakumemo-2008-06.pdf.

Figure 6. Error contours for BH spin and inner disk inclination for models 4 (left), 8 (middle), and 10 (right). The 1σ, 2σ, and 3σ contours are shown.

Table 3
Fit Parameters for Models with `kerrbb`

Parameter	Unit/Description	Model 8 Value[a]	Model 9 Value[a]
Interstellar absorption			
N_H	10^{21} cm^{-2}	6.6 ± 0.2	6.5 ± 0.1
Thermal component (`kerrbb`[b])			
i	Inclination (deg)	53.9 ± 0.4	40.4 ± 0.5
a_*	BH Spin	0.838 ± 0.006	0.973 ± 0.004
$\dot{M}$	Accretion rate (10^{18} g s^{-1})	$0.203^{+0.004}_{-0.006}$	$0.127^{+0.005}_{-0.007}$
Comptonization (`simpl`)			
Γ	Photon index	2.66 ± 0.02	2.65 ± 0.02
f_{scat}	Scattering fraction	0.104 ± 0.004	$0.10499^{+0.00344}_{-0.00001}$
E_{fold}	keV	190^{+40}_{-20}	180^{+30}_{-10}
Simple ionized absorber			
N_H	10^{22} cm^{-2}	$3.46^{+0.12}_{-0.20}$	$3.27^{+0.08}_{-0.41}$
$\log \xi$	erg cm s^{-1}	$5.00^{+0.00}_{-0.13}$	$5.0^{+0.0}_{-0.2}$
Reflection component (`reflionx_hc`)			
ξ	erg cm s^{-1}	$20,000^{+0}_{-1200}$	$19,200^{+800}_{-3700}$
Fe/solar	Abundance	$1.99^{+0.11}_{-0.22}$	$2.00^{+0.18}_{-0.14}$
N_{ref}	Normalization ($\times 10^{-6}$)	$6.45^{+0.01}_{-0.23}$	$5.9^{+1.3}_{-0.3}$
Relativistic blurring (`relconv`[c])			
q	Emissivity index	7.8 ± 0.5	$2.48^{+0.09}_{-0.05}$
Gaussian blurring (`gsmooth`)			
σ	keV	$\cdots$	$0.28^{+0.02}_{-0.04}$
Cross-normalization constants (relative to FPMA)			
C_{XIS0}	$\cdots$	1.081 ± 0.005	$1.081^{+0.002}_{-0.004}$
C_{XIS1}	$\cdots$	1.038 ± 0.004	$1.038^{+0.002}_{-0.004}$
C_{FPMB}	$\cdots$	1.001 ± 0.001	1.001 ± 0.001
C_{PIN}	$\cdots$	1.205 ± 0.007	1.205 ± 0.006
C_{GSO}	$\cdots$	1.17 ± 0.06	1.16 ± 0.06
χ^2/ν	$\cdots$	$1512/1146$	$1510/1145$

Notes.
[a] With 90% confidence errors. A value of zero for the positive error indicates that the parameter's error range reached the upper limit of values provided for the model.
[b] Fixed parameters and their values include $\eta = 0.0$, which corresponds to the zero torque inner boundary condition, $M_{BH} = 14.8\,M_\odot$, $d = 1.86$ kpc, and a spectral hardening factor of 1.7.
[c] Two other parameters in this model are the inner and outer radii from where the reflected emission is coming: R_{in} is set to be at the ISCO and $R_{out} = 400\,R_g$. The inclination and spin parameters (i and a_*) are free, but they are forced to take the same values as for `kerrbb`.

and *NuSTAR* provides a huge improvement in the statistical quality of the data, while alleviating some systematic concerns such as pile up.

We have presented fits to the spectrum with several different models and, while some parameters show significant differences, others agree about the properties of the system. It is clear that the source was in the soft state with a prominent thermal component and a power law with a photon index between $\Gamma = 2.59$ and 2.67, which meets the $\Gamma > 2.5$ criterion for Cyg X-1 to be in the soft state (Grinberg et al. 2013). There is clear evidence for absorption due to highly ionized material, which is consistent with the findings of Yamada et al. (2013). Also, the fits agree that the ionization state of the disk material that leads to the reflection component is high and that iron is overabundant by a factor of 1.9–2.9 relative to solar.

The BH spin and inclination measurements vary from model to model by more than the 90% confidence statistical errors,

indicating that there is significant systematic uncertainty. For the inclination, it is also necessary to compare our values of $i = 42°$–$69°$ with the value of $i = 27°.1 \pm 0°.8$ that is obtained by modeling optical photometric and spectroscopic measurements (Orosz et al. 2011), but the optical measurement is of the inclination of the binary while the reflection component measures the inclination of the inner part of the disk. We have shown (see Figure 4(d)) that the reflection model simply cannot reproduce an inclination as low as 27°.1.

However, we must also keep the limitations of the spectral model in mind. While the `relconv` calculation is for a specific inclination angle, `reflionx_hc` calculates the spectrum of the reflection component by averaging over angles. Another consideration is that the ionization parameter (ξ) is at the top of the available range for `reflionx_hc`. The model already includes Compton broadening of the lines, which increases with increasing ξ, but it is possible that some extra Compton broadening is necessary to account for a higher ionization. Also, surface turbulence may cause some symmetric line broadening that is not taken into account by `reflionx_hc`. To test this, we added a Gaussian convolution model (`gsmooth`), which acts on the reflection component along with `relconv`. The results are shown in Table 3, where this is listed as model 9, and the inclination decreases significantly from 53°.9 to 40°.4. The value obtained for the `gsmooth` σ parameter is $0.28^{+0.02}_{-0.04}$ keV. Using $kT = (1/2)m_e c^2(\sigma/E)^2$, where m_e is the electron rest mass, this value of σ corresponds to a temperature of $kT = 0.4$–0.6 keV at $E = 6$–7 keV, which is in line with the inner disk temperatures we obtain from the disk blackbody fits.

While adding symmetric smoothing of the iron line and reflection component (i.e., extra Compton broadening) causes a drop in i, we emphasize that asymmetric relativistic broadening is required by the data. For our original Gaussian fit to the iron line, we obtained a best-fit centroid value of 5.3 keV, which shows that the line has the low-energy tail expected for a gravitational redshift. Also, we obtained a very poor fit with `reflionx_hc` (Figure 4(b)), where the Compton broadening was already included. Adding the relativistic broadening provided a very large improvement to the fit (Figure 4(c)).

Although conclusions about the BH spin depend on the different possibilities for the inclination, the models that provide good fits to the data (models 4, 5, 8, and 9) all have $a_* > 0.83$, indicating at least relatively high spin. The best fit (model 4) also has the highest spin $a_* = 0.9882 \pm 0.0009$, but this either requires a very large warp in the accretion disk or that the binary inclination is somewhat higher than the best-fit value found in Orosz et al. (2011). We note that Table 1 in Orosz et al. (2011) reports that some of their models give significantly higher inclinations, but the χ^2 values for the higher inclination models are worse.

Another potentially interesting result that comes from this spectrum is the constraint on the emissivity profile. A comparison of models 4–6 indicate that a broken power-law emissivity is preferred as it is a very steep profile in the inner part of the disk ($q_{in} \sim 10$). For active galactic nuclei (AGNs), relatively steep profiles ($q = 4.3$–5.0) were reported for MCG–6-30-15 (Wilms et al. 2001) and steep profiles are discussed in Wilkins & Fabian (2012). Walton et al. (2013) studied a large sample of AGNs and found that steep profiles are common. This has been taken as evidence that the irradiating source comes from very close to the BH and Fabian et al. (2012b) conclude that it must lie within 1 R_g of the BH event horizon. While this may also be the case for Cyg X-1, our fits with very steep profiles (models 4,

5, and 8) also have inclinations between 53°.9 and 69°.2. Our fit with `gsmooth` (model 9) included in the model gave a much flatter index of $q = 2.48^{+0.09}_{-0.05}$, leaving open the possibility that the profile is relatively flat, in which case the source is at a height of 5–10 R_g or more.

While we cannot conclude anything definitive about the slope of the emissivity profile, if it is very steep, this might point to a "lamppost" geometry (Dauser et al. 2010), where the emission actually comes from the base of a collimated jet. This geometry may not be relevant for the soft state because there is no evidence for a jet. Despite this, if we start with model 8 but replace `relconv` with `relconv_lp` (model 10), we find $i = 41°.5 \pm 0°.5$ and $a_* = 0.953 \pm 0.006$ (see Figure 6 for the error contours), with only small changes in the other parameters. However, the quality of the fit is somewhat worse ($\chi^2_\nu = 1.44$) for model 10 compared with the models reported in Tables 2 and 3.

After exploring different continuum models, emissivity geometries, and conditions for the material in the accretion disk, we only find inner disk inclinations that are $>13°$ higher than the binary value measured by Orosz et al. (2011) and, as discussed above, one explanation is that there is a warp in the accretion disk. Analytical calculations as well as numerical simulations have shown that disk warps can occur (Bardeen & Petterson 1975; Schandl & Meyer 1994; Fragile et al. 2007) and that they should occur if the BH spin is misaligned with the orbital plane (and outer disk). As the alignment time for an accreting BH can be longer than the lifetime of a high-mass system (Maccarone 2002), if the Cyg X-1 BH formed with a misaligned spin, it would remain misaligned. If jets are aligned with the BH spin, then there is evidence for misalignment in systems like Cyg X-3, V4641 Sgr, and GRO J1655–40 (Maccarone 2002). It should be noted that Fragile (2009) has shown that, under certain assumptions about the thickness of the accretion disk, BH spin measurements using the inner radius of a warped disk can be incorrect. While a disk warp may not be the only possibility for Cyg X-1, further investigations to determine if the disk is really warped have important implications for the BH spin measurement.

5. SUMMARY AND CONCLUSIONS

We have presented a detailed study of the ~1–300 keV spectrum of Cyg X-1 in the soft state. The spectrum is complex and consists of multi-temperature blackbody, power law, and reflection components along with absorption from highly ionized material in the system. Although the observation was of moderate duration (~29 ks), *NuSTAR* provides a very high-quality and high-statistics measurement of the reflection spectrum, including an iron complex with broad emission and narrow absorption lines. We find that the reflecting material has a high ionization state, is overabundant in iron relative to solar, and requires broadening of the iron line that is well described by a relativistic blurring model.

While all models that provide a good fit to the spectrum indicate a rapidly rotating BH with $a_* > 0.83$ and our best-fitting model has $a_* = 0.9882 \pm 0.0009$ (90% confidence statistical errors only), we were not able to obtain a good fit with the inclination fixed to the Orosz et al. (2011) binary value. This may indicate a misalignment between the orbital plane and the inner accretion disk (by $>13°$), missing physics in the spectral models, or it may possibly motivate work to confirm the measurement of the binary inclination. Regardless of which of these possibilities is correct, it is clear that the combination of *NuSTAR*'s high throughput and energy resolution provides a

major advance in reflection studies, allowing for strict tests of the models, which we expect to lead to improved constraints on the physical processes at work in Cyg X-1 and other accreting BH systems.

REFERENCES

Arnaud, K. A. 1996, in ASP Conf. Ser. 101, Astronomical Data Analysis Software and Systems V, ed. G. H. Jacoby & J. Barnes (San Francisco, CA: ASP), 17
Bałucińska-Church, M., Church, M. J., Charles, P. A., et al. 2000, MNRAS, 311, 861
Bardeen, J. M., & Petterson, J. A. 1975, ApJL, 195, L65
Bowyer, S., Byram, E. T., Chubb, T. A., & Friedman, H. 1965, Sci, 147, 394
Brocksopp, C., Tarasov, A. E., Lyuty, V. M., & Roche, P. 1999, A&A, 343, 861
Cabanac, C., Fender, R. P., Dunn, R. J. H., & Körding, E. G. 2009, MNRAS, 396, 1415
Dauser, T., Wilms, J., Reynolds, C. S., & Brenneman, L. W. 2010, MNRAS, 409, 1534
Duro, R., Dauser, T., Wilms, J., et al. 2011, A&A, 533, L3
Fabian, A. C., Rees, M. J., Stella, L., & White, N. E. 1989, MNRAS, 238, 729
Fabian, A. C., Wilkins, D. R., Miller, J. M., et al. 2012a, MNRAS, 424, 217
Fabian, A. C., Zoghbi, A., Wilkins, D., et al. 2012b, MNRAS, 419, 116
Foreman-Mackey, D., Hogg, D. W., Lang, D., & Goodman, J. 2013, PASP, 125, 306
Fragile, P. C. 2009, ApJL, 706, L246
Fragile, P. C., Blaes, O. M., Anninos, P., & Salmonson, J. D. 2007, ApJ, 668, 417
Gies, D. R., & Bolton, C. T. 1986, ApJ, 304, 371
Goodman, J., & Weare, J. 2010, Commun. Appl. Math. Comput. Sci., 5, 65
Gou, L., McClintock, J. E., Reid, M. J., et al. 2011, ApJ, 742, 85
Gou, L., McClintock, J. E., Remillard, R. A., et al. 2013, ApJ, submitted (arXiv:1308.4760)
Grinberg, V., Hell, N., Pottschmidt, K., et al. 2013, A&A, 554, A88
Hanke, M., Wilms, J., Nowak, M. A., et al. 2009, ApJ, 690, 330
Harrison, F. A., Craig, W. W., Christensen, F. E., et al. 2013, ApJ, 770, 103
Kallman, T., & Bautista, M. 2001, ApJS, 133, 221
Koyama, K., Tsunemi, H., Dotani, T., et al. 2007, PASJ, 59, 23
Laor, A. 1991, ApJ, 376, 90
Lightman, A. P., & White, T. R. 1988, ApJ, 335, 57
Maccarone, T. J. 2002, MNRAS, 336, 1371
Matsuoka, M., Kawasaki, K., Ueno, S., et al. 2009, PASJ, 61, 999
McClintock, J. E., Shafee, R., Narayan, R., et al. 2006, ApJ, 652, 518
Miller, J. M. 2007, ARA&A, 45, 441
Miller, J. M., Homan, J., Steeghs, D., et al. 2006, ApJ, 653, 525
Miller, J. M., Parker, M. L., Fuerst, F., et al. 2013, ApJL, 775, L45
Miller, J. M., Pooley, G. G., Fabian, A. C., et al. 2012, ApJ, 757, 11
Miller, J. M., Wojdowski, P., Schulz, N. S., et al. 2005, ApJ, 620, 398
Mitsuda, K., Bautz, M., Inoue, H., et al. 2007, PASJ, 59, 1
Mitsuda, K., Inoue, H., Koyama, K., et al. 1984, PASJ, 36, 741
Murdin, P., & Webster, B. L. 1971, Natur, 233, 110

Nowak, M. A., Hanke, M., Trowbridge, S. N., et al. 2011, ApJ, 728, 13
Nowak, M. A., Wilms, J., & Dove, J. B. 2002, MNRAS, 332, 856
Orosz, J. A., McClintock, J. E., Aufdenberg, J. P., et al. 2011, ApJ, 742, 84
Poutanen, J., Zdziarski, A. A., & Ibragimov, A. 2008, MNRAS, 389, 1427
Reid, M. J., McClintock, J. E., Narayan, R., et al. 2011, ApJ, 742, 83
Reis, R. C., Fabian, A. C., & Miller, J. M. 2010, MNRAS, 402, 836
Remillard, R. A., & McClintock, J. E. 2006, ARA&A, 44, 49
Reynolds, C. S., & Nowak, M. A. 2003, PhR, 377, 389
Risaliti, G., Harrison, F. A., Madsen, K. K., et al. 2013, Natur, 494, 449
Ross, R. R., & Fabian, A. C. 2005, MNRAS, 358, 211
Schandl, S., & Meyer, F. 1994, A&A, 289, 149
Steiner, J. F., Narayan, R., McClintock, J. E., & Ebisawa, K. 2009, PASP, 121, 1279

Takahashi, T., Abe, K., Endo, M., et al. 2007, PASJ, 59, 35
Tomsick, J. A., Yamaoka, K., Corbel, S., et al. 2009, ApJL, 707, L87
Uchiyama, Y., Maeda, Y., Ebara, M., et al. 2008, PASJ, 60, 35
Verner, D. A., Ferland, G. J., Korista, K. T., & Yakovlev, D. G. 1996, ApJ, 465, 487
Walton, D. J., Nardini, E., Fabian, A. C., Gallo, L. C., & Reis, R. C. 2013, MNRAS, 428, 2901
Wilkins, D. R., & Fabian, A. C. 2012, MNRAS, 424, 1284
Wilms, J., Allen, A., & McCray, R. 2000, ApJ, 542, 914
Wilms, J., Reynolds, C. S., Begelman, M. C., et al. 2001, MNRAS, 328, L27
Xiang, J., Lee, J. C., Nowak, M. A., & Wilms, J. 2011, ApJ, 738, 78
Yamada, S., Torii, S., Mineshige, S., et al. 2013, ApJL, 767, L35